PHYSICAL REVIEW E **73**, 021704 (2006)

Light-induced chaotic rotations in nematic liquid crystals

E. Brasselet[1] and L. J. Dubé[2,*]
[1]*Laboratoire de Physique UMR 5672, École Normale Supérieure de Lyon, 46 Allée d'Italie, 69364 Lyon Cedex 07, France*
[2]*Département de Physique, de Génie Physique, et d'Optique, Université Laval, Cité Universitaire, Québec, Canada G1K7P4*

(Received 12 October 2005; published 23 February 2006)

Various nonlinear rotation regimes are observed in an optically excited nematic liquid-crystal film under boundary conditions (for the light and material) that are invariant by rotation. The excitation light is circularly polarized, the intensity profile is circularly symmetric, and the beam diameter at the sample location is a few times smaller than the cell thickness. A transition to chaos via quasiperiodicity is identified when the light intensity is taken as the control parameter. Transverse nonlocal effects are suggested to be the cause of the observed dynamics, and a simple model consisting of a collection of coupled rotators is developed to provide a qualitative explanation.

DOI: 10.1103/PhysRevE.73.021704 PACS number(s): 42.70.Df, 42.65.Sf, 05.45.Ac, 05.45.Tp

I. INTRODUCTION

The long-range orientational order of the molecules in liquid crystals adds a collective character to the light-matter interaction and generates a unique spatiotemporal feedback mechanism responsible for the dynamical richness of optically induced orientational phenomena. This is particularly true when the light-matter system is not invariant under rotation about the light propagation axis—e.g., elliptical polarization [1], or an asymmetric intensity profile [2] at normal incidence and ordinary waves at small oblique incidence [3], where quasiperiodic or chaotic behavior has already been reported. Such systems are not only interesting by themselves but can be viewed as suitable candidates to test experimentally generic sets of equations describing nonlinear dynamics.

For instance, chaotic rotations have retained much attention in the context of the phase synchronization of coupled chaotic oscillators [4,5] and in the study of chaotic bounded flows [6]. Since the dynamics of a number of well-known systems can be reduced to a chaotic rotation (e.g., the Rössler and Lorenz systems), the study of real systems that exhibit chaotic rotations is of special interest. Quite recently, the chaotic rotation generated by light in a nematic liquid-crystal (NLC) film has been observed [2]. The light was circularly polarized with an astigmatic intensity profile, and the existence of a chaotic rotation of the director (i.e., the unit vector $\boldsymbol{n}$ that defines the local orientation of the optical axis of the NLC) has been ascribed to the rotational asymmetry arising from the astigmatism of the excitation beam [2].

In the present contribution, we show that complex and intriguing reorientation dynamics can also be generated even in the presence of rotational invariance. The interaction geometry corresponds to a light beam with circular polarization and a circularly symmetric intensity profile focused on a homeotropic nematic liquid-crystal film. The director trajectory is reconstructed solely from the experimental data obtained from the analysis of the light at the output of the sample. We observe the following sequence of distinct dynamical regimes when the light intensity, taken as the control parameter, is increased: periodic, quasiperiodic, chaotic, quasiperiodic, periodic. The appearance of this scenario is ascribed to the use of a beam diameter a few times smaller than the cell thickness. The competition between finite beam size effects and spin angular momentum transfer to the medium will also be discussed.

The paper is organized as follows. In Sec. II, the experimental procedure is described together with the observed dynamical scenario. This is then followed by a detailed linear and nonlinear analysis of time series reconstructed from experimental intensity observations. In Sec. III, we briefly compare our results with those of previous studies and point out the importance of a critical geometrical aspect ratio (excitation beam diameter over cell width) below which complex dynamics is produced. We also construct a Kuramoto-like model to account qualitatively for the appearance of a critical aspect ratio associated with finite beam effects. We finally collect our conclusions in the last section.

II. EXPERIMENTS AND TIME SERIES ANALYSIS

A. Experimental procedure and dynamical scenario

Our observations concern a homeotropically aligned NLC cell illuminated by a circularly polarized laser beam operating at 532 nm in the fundamental mode TEM_{00} whose Gaussian intensity profile is written $I(x,y)=I_0\exp[-2(x^2+y^2)/w_0^2]$. The light beam is focused on the sample by means of a lens with focal length 150 mm at normal incidence (along the z axis). The beam diameter $2w_0$, at e^{-2} of maximum intensity at the sample location, is measured to be 30 μm and the cell thickness is $L=75$ μm. The experimental setup is shown in Fig. 1. It permits the monitoring of the director dynamics via the real-time acquisition of the total intensity I_c of the central part of the emerging excitation beam (placing a diaphragm at the output of the sample) and the intensities of the horizontal and vertical components of

---

[*] Also at Laboratoire de Chimie-Physique-Matière et Rayonnement, Université Pierre et Marie Curie, Paris, France.

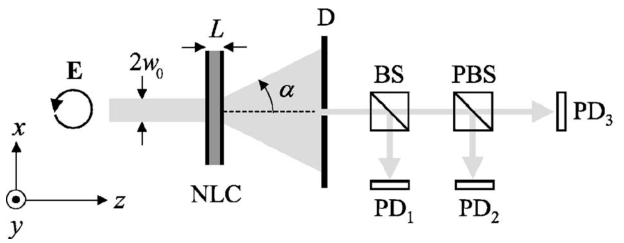

FIG. 1. Sketch of the experimental setup. $2w_0$ is the beam diameter defined at e^{-2} of its maximal intensity; **E**, circularly polarized incident electric field; NLC, nematic liquid-crystal film of thickness L; D, diaphragm; BS, beam splitter; PBS, polarization beam splitter; PD_i, photodiodes. The angle α is the divergence angle of the beam after its passage through the reoriented film resulting from self-focusing effects. This angle may be tens of degrees in the strongly reoriented states ($\Theta_{\max} \simeq 1$). The photodiode PD_1 collects the intensity I_c, which is proportional to the total intensity emerging from the diaphragm, and $\mathrm{PD}_{2,3}$ collect the intensities $I_{x,y}$ of the horizontal and vertical components of the electric field.

the electric field, I_x and I_y ($I_c = I_x + I_y$). This setup has been originally used in a previous study [7] where it is explained that, on the one hand, the time series $I_c(t)$ contains explicit information on Θ only and that, on the other hand, the time series $I_x(t)$ and $I_y(t)$ contain explicit information on both Θ and Φ where Θ and Φ are, respectively, the polar and azimuthal angles of the reorientation of the director, $\boldsymbol{n} = (\sin\Theta\cos\Phi, \sin\Theta\sin\Phi, \cos\Theta)$. The normalized intensities with respect to I_c, $i_x(t) \equiv I_x/I_c$ and $i_y(t) \equiv I_y/I_c$, contain for their part only explicit information on Φ. Since $i_x(t) = 1 - i_y(t)$, these time series possess the same dynamical information and we shall refer to any one of them as $i(t)$.

In the present work we propose to reconstruct the director trajectory in the (x,y) plane solely from the experimental quantities $I_c(t)$ and $i(t)$. For this purpose, we define a mathematical object $(\tilde{n}_x, \tilde{n}_y) = (\tilde{n}_\perp \cos\tilde{\Phi}, \tilde{n}_\perp \sin\tilde{\Phi})$ which embodies the dynamics of the physical director. From the above considerations, the azimuthal degree of freedom $\tilde{\Phi}$ is reconstructed from the time series $i(t)$, whereas we choose

$$\tilde{n}_\perp(t) = I_c(t). \tag{1}$$

Strictly speaking, this quantity is to be kept distinct from the projection of the real director $n_\perp$ onto the (x,y) plane. In fact, the larger the director's reorientation angle (i.e., $n_\perp$), the lower is the intensity in the central part of the output beam (i.e., $\tilde{n}_\perp$) and the relationship between the two quantities is not simple. However, only the fact that $\tilde{n}_\perp$ and $n_\perp$ contains the same dynamical features is of interest in the present context.

Next, we calculate the time delay τ_d as the first zero of the autocorrelation function $C(f,\tau) = T^{-1}\int_0^T F(t)F(t+\tau)dt$ where T is the duration of the time series $f(t)$ (typically $T \sim 10^4$ s) and $F(t) = f(t) - T^{-1}\int_0^T f(t)dt$ is the zero-mean-value part of $f(t)$. Since there is no possible ambiguity, we will further keep the notation i and I_c to mean that the zero-mean-value parts are used [e.g., in Eq. (2) or Figs. 5 and 6]. Finally, $\tilde{\Phi}$ is defined as

$$\tilde{\Phi}(t) = \arctan\left[\frac{i(t+\tau_d)}{i(t)}\right]. \tag{2}$$

Figure 2 shows the time evolution of $\tilde{n}_\perp$ (left column) and $\tilde{\Phi}$ (center column). The director dynamics in the plane $(\tilde{n}_x, \tilde{n}_y)$ is presented on the right-hand side of the figure. The excitation intensity is progressively increased starting from the unperturbed state [i.e., $\rho < 1$ where $\rho = I/I_F$ is the light intensity I normalized to the optical Fréedericksz transition threshold (OFT) value I_F]. The sampling time is $\Delta t = 0.25$ s, which is more than one order of magnitude smaller than the characteristic reorientation time of the cell estimated to be $\tau_{\mathrm{NLC}} \simeq 5$ s. The complete experiment lasted up to 20 h without anchoring breakdown, which enables data acquisition during several hours for each value of the intensity, at a fixed point of the sample. Time series with duration 10^4 s have then been extracted for each regime to plot the director trajectories in the plane $(\tilde{n}_x, \tilde{n}_y)$. Since the long-term behavior of the azimuthal angle is always a quasiuniform precession around the light propagation axis (z), one can write

$$\tilde{\Phi}(t) = \Omega t + \Psi(t). \tag{3}$$

The angular velocity Ω corresponds to a long-term uniform precession of the director around the z axis whereas $\Psi(t)$ describes the nonuniform part of the azimuthal dynamics, as can be seen in the insets of $\tilde{\Phi}(t)$ in Fig. 2. The director dynamics amounts therefore to nonlinear rotations, and the observed five distinct regimes are labeled Rn (n=1, 2, 3, 4, and 5) for intensities ρ=1.10, 1.31, 1.53, 1.63 and 1.72, respectively. The right column of Fig. 2 shows these different director trajectories in red (online), for typical temporal windows of duration $2\pi/\Omega$. Regimes R1, R2, and R3 correspond to small reorientation amplitude (i.e., the maximum reorientation amplitude $\Theta_{\max}$ satisfies $\Theta_{\max}^2 \ll 1$), where only one self-diffraction ring [8] is observed at the maximum with $\Theta_{\max}^2 \simeq 0.1$. In contrast, regimes R4 and R5 exhibit several rings (up to 20) and correspond to strongly reoriented states ($\Theta_{\max} \simeq 1$).

The observed sequence of regimes differs from the one predicted by the infinite plane-wave model where instead a sequence of type R1→R2→R5 is predicted [9]. The unexpected regimes R3 and R4 can thus be attributed at first sight to finite beam size effects as suggested by our preliminary observations [7]. We will next characterize the sequence of nonlinear rotations Rn with a detailed (linear and nonlinear) time-series analysis.

B. Data analysis

1. Linear measures

We have selected three linear indicators to begin the analysis of the time series: namely, the evaluation of Ω [which is obtained by fitting $\tilde{\Phi}(t)$ to a linear function], the autocorrelation function, and the Fourier power spectrum for the time series $I_c(t)$ and $i(t)$ for each rotating regime Rn (n

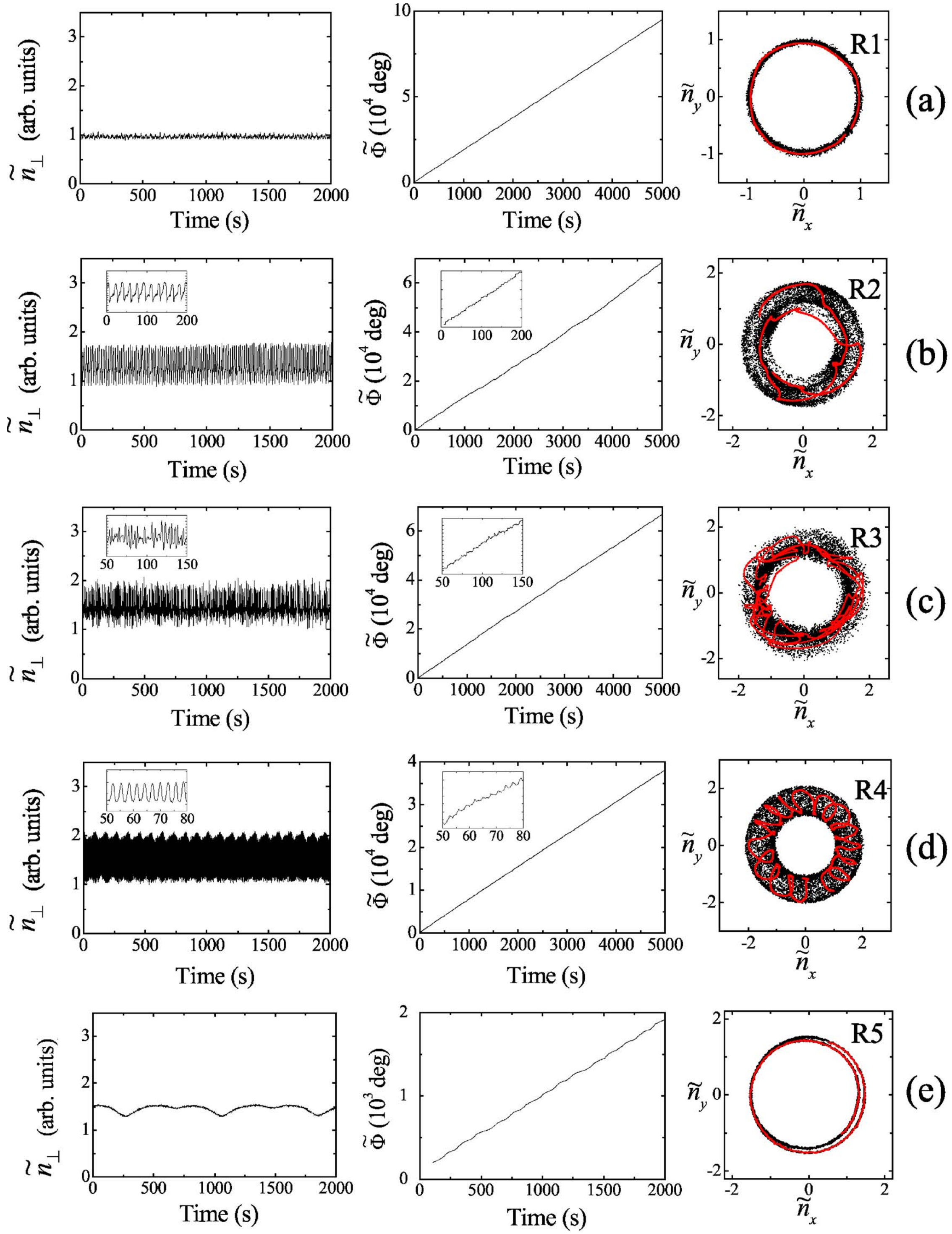

FIG. 2. (Color online) Experimental director dynamics of the rotating regimes. The left column displays the time series $\tilde{n}_\perp(t)$, the center one shows $\tilde{\Phi}(t)$, and the right column is the director trajectory in the $(\tilde{n}_x,\tilde{n}_y)$ plane. (a) R1 at $\rho=1.10$, (b) R2 at $\rho=1.31$, (c) R3 at $\rho=1.53$, (d) R4 at $\rho=1.63$, and (e) R5 at $\rho=1.72$. Trajectories for a short temporal window appear (in red online) the right column.

$=1$, 2, 3, 4, and 5). From Table I, we see that the averaged precession rate Ω is a decreasing function of n, which indicates that the averaged reorientation angle Θ increases with intensity (the viscous torque scales as $\sin^2\Theta$). The almost periodic rotating regimes R1 and R5 thus differ only by their characteristic time scale, the precession rate of R5 being approximately 20 times smaller than that of R1. One notices also a small residual synchronous nutation in R1 [see Fig. 5(b) below], and R5 [see Fig. 2(e)]. In distinction, a nutation motion ($\partial_t\Theta \neq 0$) is coupled to precession for the R2, R3, and R4 regimes, as indicated by a thickening of the trajectory in the (x,y) plane. Obviously, these three regimes are qualitatively different as seen from the short-time trajectories shown in Fig. 2: regime R3 looks particularly irregular [see

TABLE I. Linear and nonlinear dynamical characteristics of rotating regimes R1, R2, R3, R4, and R5: angular velocity Ω, autocorrelation times τ_c of the time series $I_c(t)$ and $i(t)$, and converged correlation dimension $\bar{d}_2$ for the time series $i(t)$.

Regime	Ω (deg/s)	$\tau_c[I_c]$ (s)	$\tau_c[i]$ (s)	$\bar{d}_2[i]$
R1	19.1		5100	1.16±0.13
R2	13.8	160	810	1.99±0.07
R3	13.1	12	400	2.22±0.17
R4	7.56	200	7800	1.47±0.04
R5	0.91			

the inset of $\tilde{n}_\perp(t)$ in Fig. 2(c)] whereas regime R4 exhibits a rather regular precession-nutation motion of the director with two distinct frequencies $f_{\text{precession}}$ and f_{nutation} with $f_{\text{nutation}}/f_{\text{precession}} \simeq 17$. The uniform nature of the nutation motion is emphasized by the almost sinusoidal oscillations of $\tilde{n}_\perp(t)$ [see the inset of Fig. 2(d)]. Regime R2 also corresponds to a quasiperiodic precession-nutation motion characterized by $f_{\text{nutation}}/f_{\text{precession}} \simeq 1.5$. However, the nutation is clearly nonlinear as evidenced by the presence of harmonics in the time behavior of $\tilde{n}_\perp(t)$ [see the inset of in Fig. 2(b)].

The autocorrelation functions $C(f,\tau)$ of the sequences R2, R3, and R4 (Fig. 3) reveal further distinctive features of the three regimes. For instance, they are each characterized by a distinct pair of autocorrelation times $\{\tau_c[i],\tau_c[I_c]\}$ (Table I) where $\tau_c[f]$ is estimated as the time when the envelope of $C(f,\tau)$ has fallen by a factor of 10. At least one correlation time of each pair varies by one order of magnitude (or more) for any combination of regimes $\{\mathrm{R}i,\mathrm{R}j\}$ $(i,j=1,2,3)$. The sudden decrease of $\tau_c[I_c]$ as one goes from R2 to R3 indicates that a drastic broadening must have occurred in the Fourier spectrum of $I_c(t)$ associated with the appearance of new frequencies. This is confirmed in Fig. 4 where the power Fourier spectra are plotted for the regimes R2, R3, and R4. The relative importance of low frequencies in the R3 regime suggests that a transition to a very irregular regime (still to be characterized) has occurred between R2 and R3. The further disappearance of the low-frequency background at higher intensity (R4 regime) demonstrates the intrinsic nonlinear nature of the R3 dynamics and rules out the appearance of an experimental noise caused by the irreversible degradation of the anchoring condition and of the integrity of the nematic film.

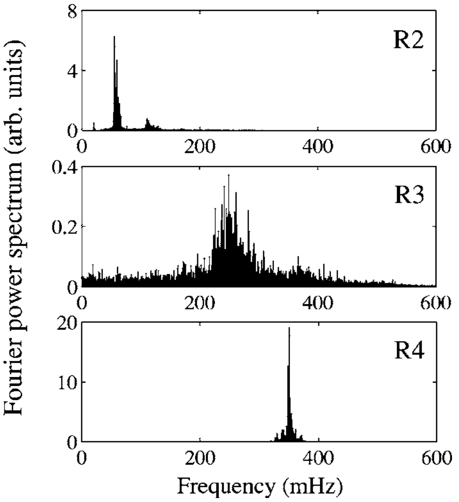

FIG. 4. Power Fourier spectrum of the noise-reduced time series $I_c(t)$ in regimes R2, R3, and R4 (see Sec. II B 2 for details of the noise-reduction procedure).

In this respect, we note that in the context of optically generated nonlinear dynamics in nematic liquid crystals, anchoring problems have been found to be a severe limitation to the acquisition of long-time series (several hours) [2,10]. In contrast, we have observed the sequence of bifurcations associated with the regimes Rn without any damage of the

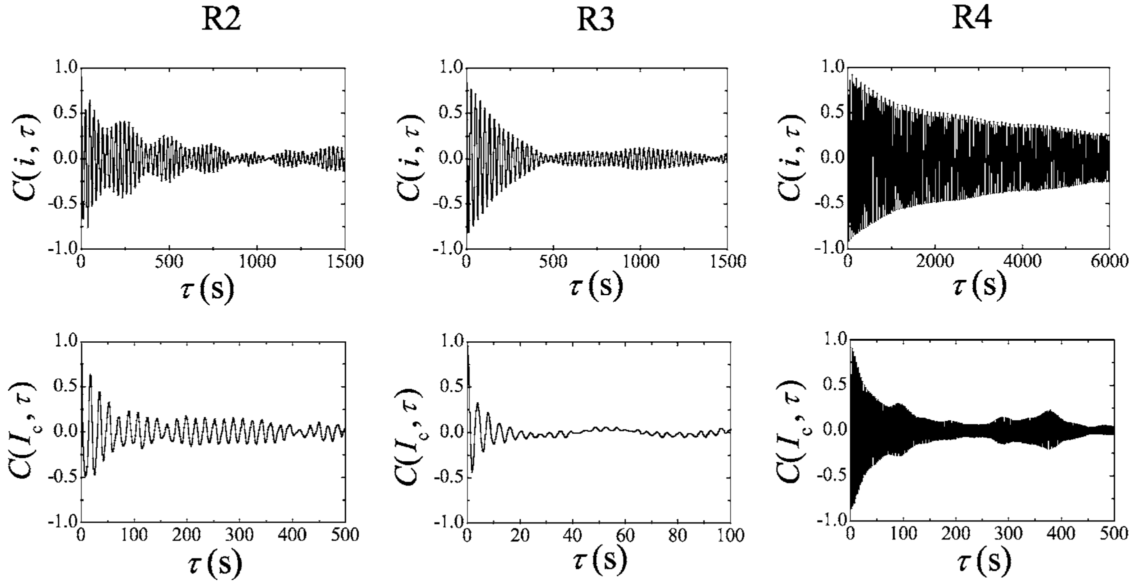

FIG. 3. Autocorrelation functions for the normalized intensity i (upper graphs) and I_c (lower graphs) in regimes R2, R3, and R4 (from left to right).

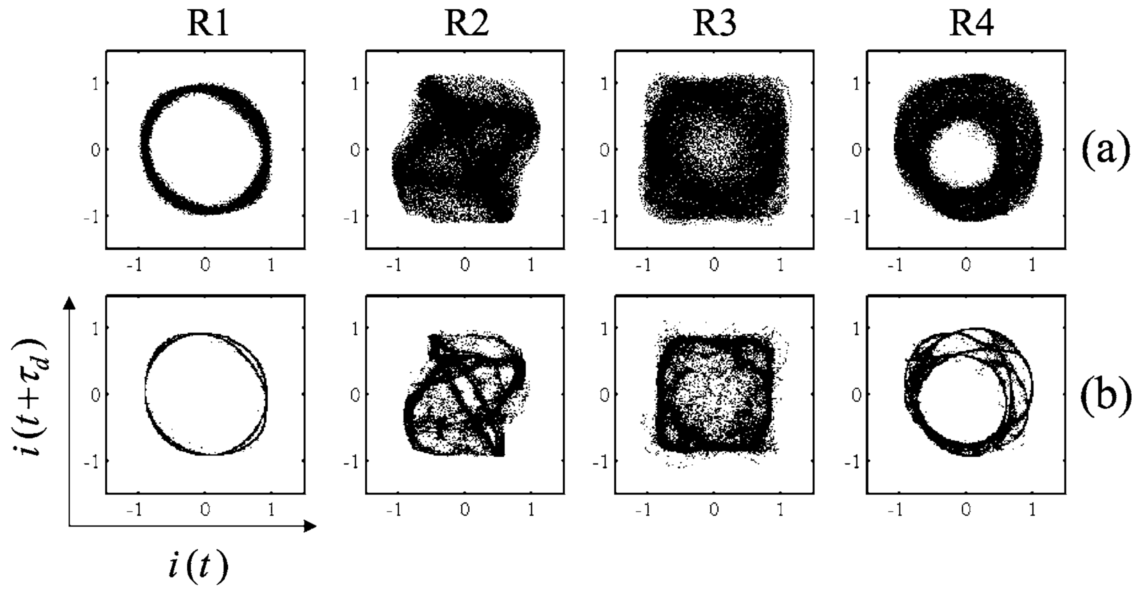

FIG. 5. Reconstructed phase space $i(t+\tau_d)$ versus $i(t)$ of regimes R1, R2, R3, and R4. (a) Original data and (b) noise-reduced data.

anchoring, which has allowed us to obtain time series of several hours for each intensity in a single experiment (the complete experiment lasted up to 20 h). Our ability to do so lies in the fact that the R3 regime is associated with a small reorientation amplitude whereas, in other interaction geometries, the strongly reoriented (several self-diffraction rings) director dynamics tends to prematurely wear the system out and the anchoring eventually breaks down [2,10].

To get a further grasp on the characteristics of the different regimes, and especially to identify the complex R3 dynamics as chaos, we now turn to the tools of nonlinear analysis.

2. Nonlinear measures

Although visual irregularity and spectral broadening are necessary indices for the presence of chaotic dynamics, they are not sufficient to distinguish a complicated signal from a chaotic one. The nonlinear analysis toolbox has matured considerably during the past decades [11], and some of the methods are becoming standard and useful when employed with the necessary care.

First, the presentation of our data as a return map, $x(t+\tau_d)$ versus $x(t)$ (where $x=i$ or I_c), offers an image of the dynamics that is complementary to the ones shown in Fig. 2. Figures 5(a) and 6(a) display the original data with a delay time τ_d chosen customarily, albeit somewhat arbitrarily, as the first zero of the autocorrelation function (see Fig. 3): for $x=i$ we have τ_d=5, 6.5, 6.5, and 12 s and for $x=I_c$, τ_d=1.5, 3.8, 1 and 1 s for the regimes R1, R2, R3, and R4, respectively. Figures 5 and 6 confirm what we have learned from the linear analysis: that a transition in the dynamical character takes place from R2 to R4. For the sequence $I_c(t)$, a

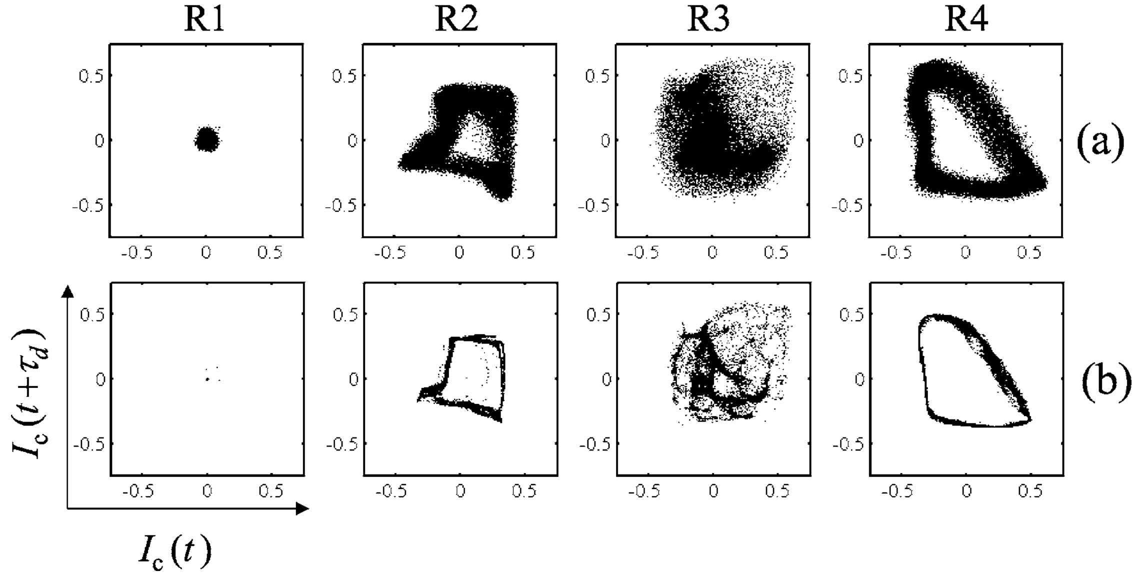

FIG. 6. Reconstructed phase space $I_c(t+\tau_d)$ versus $I_c(t)$ of regimes R1, R2, R3, and R4. (a) Original data and (b) noise-reduced data.

two-dimensional phase space seems almost sufficient to unfold the resulting structures in R2 and R4 whereas the R3 regime is higher dimensional. Similarly, for the sequence $i(t)$, the two-dimensional unfolding gives rise to well-defined manifolds in R1 and R4, in contrast to regimes R2 and R3 which exhibit a more complex organization.

In order to quantify the complexity of the system, we build, from the scalar time series $\{x_j, j=1,2,\ldots,N\}$ [$x_j = x(j\Delta t)$ where Δt is the sampling time], a set of time-delay vectors

$$\mathbf{X}_j = (x_j, x_{j+n_d}, \ldots, x_{j+(d_E-1)n_d}), \tag{4}$$

with $\tau_d = n_d \Delta t$ in a reconstructed state space of embedding dimension d_E. Embedding theorems [12,13] guarantee that, for a reasonable delay and a large enough d_E, the procedure leads to a faithful representation of the underlying system. The vectors $\mathbf{X}_j$ can then be used to calculate a dimension estimate via the correlation sum $C_2(\mathbf{X},\epsilon)$ whose practical implementation can be written as [11]

$$C_2(\mathbf{X},\epsilon) = \frac{2}{(N-n_{\min})(N-n_{\min}-1)} \times \sum_{i=1}^{N} \sum_{j=i+1+n_{\min}}^{N} \mathcal{H}(\epsilon - \|\mathbf{X}_j - \mathbf{X}_i\|), \tag{5}$$

where $\mathcal{H}$ is the Heaviside function. The expression is simply the fraction of all possible pairs of points which are closer than a given distance ϵ in a particular norm. A technical point in this implementation is the removal of pairs in a time window $t_{\min} = n_{\min}\Delta t$ in order to avoid artifacts from temporal correlations. In the limit of an infinite amount of data ($N \to \infty$) and for small ϵ, we expect C_2 to scale as $C_2(\mathbf{X},\epsilon) \propto \epsilon^{d_2}$, thereby defining the correlation dimension d_2. In practice, d_2 is obtained on a log-log plot as the slope of C_2 versus ϵ within the scaling range. We have carried out the calculations of these estimates for the different regimes and for the sequences $i(t)$ and $I_c(t)$ in embedding dimensions $d_E = 1,\ldots,7$.

Figure 7 displays a typical result for C_2 and d_2 in regime R2 for the $i(t)$ sequence. The calculations on the original data (open circles) indicate that the correlation dimension d_2 keeps increasing with embedding dimension d_E [Fig. 7(b)]. The slopes of C_2 are obtained in a scaling range centered around $\epsilon \sim 10^{-1}$ (which is approximately 1/10 of the size of the attractor). This behavior is not specific to the R2 regime or to the choice of the sequence i and is traceable to the presence of noise in the data invading the higher dimensions of the underlying lower-dimensional system. At this point, no reliable estimate of d_2 can be given.

We have then applied a nonlinear noise-reduction algorithm to the original data. For our purpose, a few experimentations have shown the simplest noise-reduction method proposed by Schreiber [14] to be quite effective. It consists basically, apart from implementational details, in the replacement of $\mathbf{X}_i$ by an average over its neighbors—i.e.,

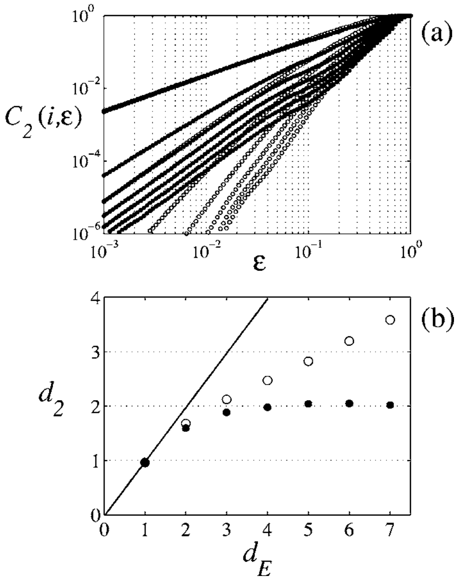

FIG. 7. (a) Correlation sum C_2 of the time series $i(t)$ as a function of the separation distance ϵ in regime R2, for embedding dimensions $d_E=1$ (top curve),…,7 (bottom curve). (b) Corresponding correlation dimension d_2 as a function of the embedding dimension d_E. Open circles refer to original data while solid circles refer to noise-reduced data. The solid curve in (b) is the line $d_2 = d_E$.

$$\mathbf{X}_i \to \tilde{\mathbf{X}}_i = \frac{1}{N_i(\epsilon)} \sum_{j=1}^{N_i(\epsilon)} \mathbf{X}_j, \tag{6}$$

where $N_i(\epsilon)$ is the number of neighbors of $\mathbf{X}_i$ within a distance ϵ. This algorithm can be iterated (typically 4–6 times) until no further corrections are applied. We have fixed the number of iterations to 5 and have checked that the main features of the power spectrum are not washed out by the procedure. The resulting noise-reduced data appear in Figs. 5(b) and 6(b) where the main features are nicely sharpened as a qualitative indicator of the noise reduction. The success of the operation is also gauged by an enlarged scaling region of the correlation sum. This is clearly seen in our illustrative example. Figure 7(a) shows as solid circles the calculations repeated on the noise-reduced data: the scaling range now extends over two orders of magnitude roughly for $\epsilon \sim 10^{-3}-10^{-1}$. Furthermore, the correlation dimension d_2 saturates rapidly as a function of d_E towards a value close to 2.

Our dimension results for all four regimes of the noise-reduced sequence $i(t)$ appear in Fig. 8. They reflect nicely the visual impression obtained by a look at Figs. 5(b) and 6(b): R1 and R4 are the low-dimensional regimes, and R2 and R3 give a comparable state-space dimension with a slight edge for R3 which is still more complex. The average correlation dimension $\bar{d}_2$ is tabulated in Table I: for R1 and R4 (R2 and R3) the average is taken over $2 \leqslant d_E \leqslant 7$ ($3 \leqslant d_E \leqslant 7$) and the error bars indicate the standard deviation about the mean. Thus far, it is safe to attribute the label quasiperiodic for regimes R2 ($\bar{d}_2 \simeq 2.0$) and R4 ($\bar{d}_2 \simeq 1.5$). In

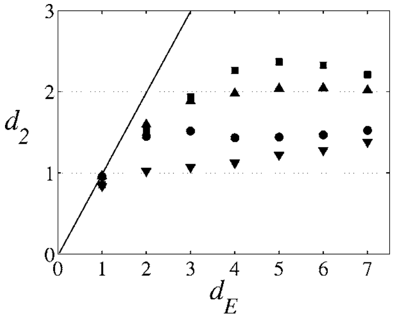

FIG. 8. Correlation dimension d_2 as a function of the embedding dimension d_E of regimes R1 (down triangles), R2 (up triangles), R3 (squares), and R4 (circles) for the noise-reduced time series $i(t)$. The solid curve corresponds to the line $d_2 = d_E$.

contrast, a further quantitative measure is needed to classify R3 ($\bar{d}_2 \simeq 2.2$).

This brings us to possibly the best evidence for chaos: namely, a positive Lyapunov exponent. If $\mathbf{X}(t)$ is the time evolution of some initial condition $\mathbf{X}(0)$ in the appropriate phase space, the largest Lyapunov exponent $\lambda_{\max}$ is found with probability 1 by

$$\lambda_{\max} = \lim_{t\to\infty} \lim_{\epsilon\to 0} \frac{1}{t} \ln\left(\frac{\|\mathbf{X}(t) - \mathbf{X}_\epsilon(t)\|}{\epsilon} \right), \tag{7}$$

with $\|\mathbf{X}(0) - \mathbf{X}_\epsilon(0)\| = \epsilon$. As an estimator, we have implemented the algorithm introduced by Rosenstein *et al.* [15] and Kantz [16]. The computation is based on the quantity

$$S(n) = \frac{1}{N} \sum_{i=1}^{N} \ln\left(\frac{1}{N_i(\epsilon)} \sum_{j=1}^{N_i(\epsilon)} \|\mathbf{X}_{i+n} - \mathbf{X}_{j+n}\| \right), \tag{8}$$

where the expression in parentheses is simply the averaged distance after a time $t_n = n\Delta t$ between initial neighbors at $t = 0$. The numerical value for $\lambda_{\max}$ is then the slope of $S(n)$ versus n in an intermediate range of n.

Based on the preceding evidence, we concentrate our attention on the sequence $I_c(t)$ for the detection of a possible chaotic rotation. It is also the sequence that shows the sharper transition from regular to chaotic dynamics [see Figs. 4 and 6(b)]. The expansion sums $S(n)$ for R2, R3, and R4 are displayed in Fig. 9. The functions are followed to saturation where the distance can no longer grow, having reached the size of the attractor. These are typical results obtained with $d_E = 4$ and $\epsilon = 0.02$. Curves for $4 \leqslant d_E \leqslant 7$ and $0.01 \leqslant \epsilon \leqslant 0.08$ are almost identical. The only remaining arbitrariness is to select the scaling range where the slopes will be calculated. There is no definitive criterion for doing this, and we have adopted the following recipe, which appears quite robust in all the cases that we have examined. We record the value $S_{\min} = S(n_d)$ and $S_{\max} = S(n \gg n_d)$ for an interval $\Delta S = S_{\max} - S_{\min}$ and define the lower bound $S_- = S_{\min} + \Delta S/4$ and the upper bound $S_+ = S_{\max} - \Delta S/4$ corresponding to abscissas n_- and n_+ between which the slope is drawn. Note that $S_{\min}$ is associated with a temporal distance $\tau_d = n_d \Delta t$, discarding the first few time steps, to allow the difference vectors between neighbors to turn towards the more unstable direction and thereby for the linear increase of $S_{\min}$ to be a proper characteristic of the exponential divergence of adjacent trajectories. To remove the final arbitrariness, we have chosen $n_d = 1$ in all of our Lyapunov exponent calculations. This leads to reproducible and conservative results. In comparison with evaluations on known dynamics, our method tends to underestimate the chaotic regimes while overestimating the more regular ones.

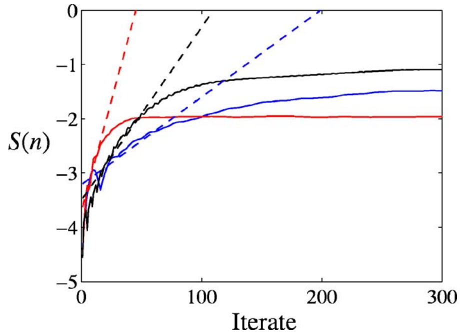

FIG. 9. (Color online) Expansion sum S as a function of the iterate in time series I_c of regimes R2 (blue online), R3 (red online), and R4 (black). The dashed curves are the linear fits in the intermediate region corresponding to $[S_-, S_+]$ as defined in the text.

In view of the procedure employed, one should therefore not put too much importance on the absolute value of $\lambda_{\max}$, but rather on what it tells us about the relative chaoticity of the different regimes. We find, for R2, R3, and R4, $\lambda_{\max} \simeq 0.06$, 0.33, and 0.13 s^{-1}, respectively (note that the unit differs from that of Table II). These values should further be compared with that of the most periodic sequence—namely, that of $i(t)$ in the R1 regime—which should set a reference value λ_0 ideally equal to zero. We obtain $\lambda_0 \simeq 4 \times 10^{-3}$ s^{-1}, two orders of magnitude smaller than that of the R3 regime. This conclusively identifies R3 as a chaotic regime.

III. DISCUSSION

A. Comparison with previous studies

There are very few reported cases of experimental observation of optically induced chaotic oscillations in NLC. One example is the case of an s-polarized laser beam at small incidence angle [10,17–19]. In this geometry, a recent numerical analysis succeeded to recover all the qualitative experimental features of the dynamics [3]. Another example is the situation of a circularly polarized light beam at normal incidence having an asymmetric intensity profile [2], for which a chaotic dynamics has been identified. Finally, irregular oscillations have also been observed in the case of a linearly polarized light beam at normal incidence with an elliptical intensity profile whose major axis is orthogonal to the electric field's direction [20]. However, no quantitative characterization of possible chaoticity is available in the latter case. Except for the case of the s-polarized excitation beam at oblique incidence, the transition to chaos still poses a challenge to a theoretical description in other situations since none of the available results, including ours, can be explained at present.

TABLE II. Comparison of chaotic rotation regime R3 to other works where a chaotic dynamics of the director have been observed. λ_0 is the maximal Lyapunov exponent in the fundamental periodic regime (R1 in our case), $\lambda_{\max}$ is the maximal Lyapunov exponent in the chaotic regime (R3 in our case), and $\bar{d}_2$ the converged value of the correlation dimension. When the parameter $\delta=2w_0/L$ is multivalued, the values correspond to its minimum and maximum, respectively. An empty entry indicates that the corresponding information is not available.

Reference	Polarization	Beam shape	δ	λ_0 ($\tau_{\rm NLC}^{-1}$)	$\lambda_{\max}$ ($\tau_{\rm NLC}^{-1}$)	$\bar{d}_2$
[17]	Oblique *o*-wave	Circular	1	2.5×10^{-3}	$\geqslant 0.2$	3.35
[10]	Oblique *o*-wave	Circular	0.93	5.6×10^{-5}	5.6×10^{-3}	
[2]	Circular	Elliptical	0.32/3.2	2.5×10^{-3}	$\geqslant 8.2\times10^{-3}$	3.50 ± 0.05
Present work	Circular	Circular	0.4	2.3×10^{-2}	1.85	2.22 ± 0.17

Table II compiles existing experimental results concerning chaotic dynamics obtained in different interaction geometries with different cell thickness L and beam diameter $2w_0$ (at e^{-2} for a Gaussian intensity profile). To allow for proper comparison, we introduce the dimensionless geometrical parameter $\delta=2w_0/L$ and give the Lyapunov exponents in normalized units ($\tau_{\rm NLC}^{-1}$). The absence of a converged value for the correlation dimension d_2 in [10] could be explained by the occurrence of a non-negligible signal-to-noise ratio in the recorded time series, as suggested by our own results where a noise reduction procedure has been shown necessary. Where convergence has been reached, the quoted values of $\bar{d}_2$ obtained in other geometries are typically larger by one unit from our reported value. The significance of this difference is difficult to assess since no details of the evaluation procedure is given; nor is any mention made of the treatment (if any) of the experimental noise. It would be premature therefore to conclude that a different underlying physical mechanism is at work in these experiments, although the interaction geometries in Refs. [17,2] surely play a role. Despite these remarks, all the experiments of Table II identify clearly a chaotic regime with a maximal Lyapunov exponent $\lambda_{\max}$ exceeding the reference value λ_0 of the most regular periodic regime by a factor of 10–100.

There are also striking similarities between our results and those of Vella *et al.* [2] concerning the regime of chaotic rotations by comparing the graphs related to R3 in Fig. 2 and Figs. 1(a), 1(c), and 1(d) of Ref. [2]. Obviously the interaction geometries are different: only the spin part of angular momentum of the incident photons is involved in the present work whereas both orbital and spin angular momenta play a role when complex dynamics is observed in Ref. [2]. This situation is depicted in Fig. 10 where the pure spin case [panel (a)] corresponds to the ratios $\delta_{x,y}=2w_{x,y}/L=3.2$ and the spin-orbital case [panel (b)] corresponds to the ratios $\delta_x=0.32$ and $\delta_y=3.2$. Vella *et al.* [2] concluded that the complexity arises from the competition between the orbital and spin angular momenta of light. However, our results, obtained with $\delta_{x,y}=0.4$ [panel (c)], do not involve the orbital part of the angular momentum of light and invite us to reconsider the interpretation of Ref. [2]. In addition, the parameter δ has already been identified to gauge the finite size effects on the reorientation dynamics [7,21]. Therefore we believe that the results of Ref. [2] could be attributed, at least in part, to finite beam size effects rather than a competition between the spin and orbital components of the light angular momentum.

We have also found that kinks may appear in the azimuthal dynamics during the nonlinear rotation regimes, as indicated by the arrows in Fig. 11 for regime R2. Again, this behavior is reminiscent of that appearing in the work of Vella *et al.* [compare their Figs. 2 and 1(b) to our Figs. 11(a) and 11(b)]. Since R2 is obviously a quasiperiodic regime, this intermittent behavior is not specifically related to the existence of chaotic dynamics. We did not study extensively the distribution of these kinks as done in Ref. [2], but the above discussion leads us to infer that their appearance could also be attributed to finite beam size effects.

In the next section, we derive a simple model that emphasizes the role of transverse nonlocal effects in the optically induced reorientation dynamics of NLC under a light beam of finite extent. It will be shown that the parameter δ can indeed be viewed as a suitable control parameter, and we determine the existence of a critical value δ_c under which the dynamics is much enriched.

B. Kuramoto-like model

The experiments have implicitly revealed the existence of a characteristic value δ_c below which dynamical regimes occur that have no counterpart in the infinite plane-wave (IPW) limit. The situation can be qualitatively analyzed with the introduction of the electric coherence length estimated at the

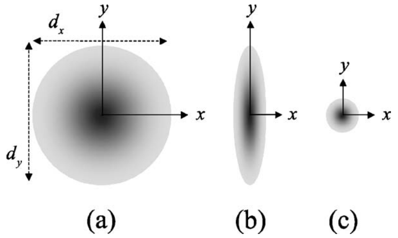

FIG. 10. Relative intensity profiles in various contexts, d_x and d_y being the diameters at e^{-2} of the maximum intensity value in the x and y directions, respectively. The scale is almost the same in the three panels. (a) Circularly symmetric situation in [2] ($\delta_x=\delta_y=d_x/L\sim3.2$). (b) Asymmetric situation in [2] ($\delta_x=d_x/L\sim0.32$, $\delta_y=d_y/L\sim3.2$). (c) Present work ($\delta_x=\delta_y=0.4$).

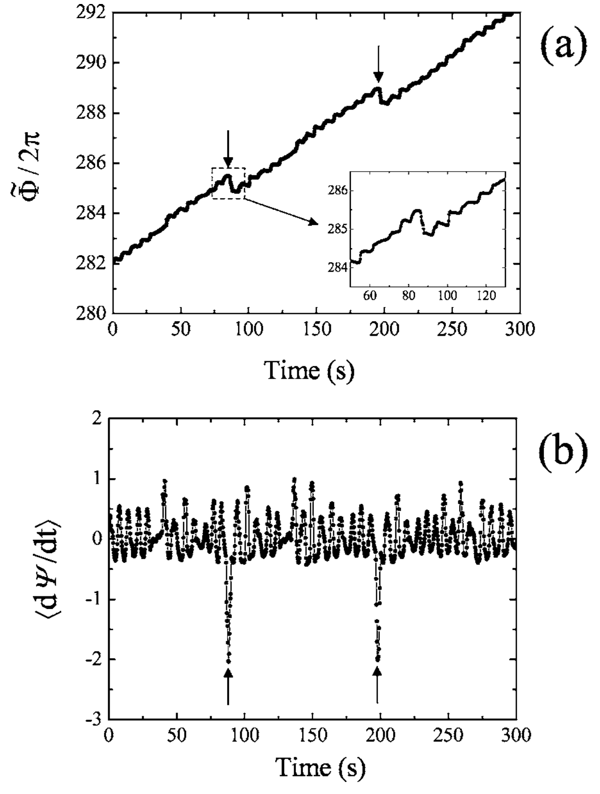

FIG. 11. (a) Kinks (indicated by arrows) during the long-term quasiuniform rotation in regime R2. (b) Time dependence of the nonuniform part of the angular velocity $d\Psi/dt$ averaged over a duration of 2 s.

OFT threshold intensity I_F: namely, $\xi=(2Kc\epsilon_\perp^{1/2}/\epsilon_a I_F)^{1/2}$ [22], where K is the Frank elastic constant in the one-constant approximation and $\epsilon_\parallel$ ($\epsilon_\perp$) is the dielectric susceptibility at optical frequency along (perpendicular to) the molecular axis, with $\epsilon_a=\epsilon_\parallel-\epsilon_\perp$. ξ implicitly depends on the parameter δ via the threshold intensity $I_F=I_F^{\mathrm{IPW}}[1+2^{3/2}/(\pi\delta)]^2$, which is the analytical expression originally derived by Zolot'ko *et al.* in the case of linear polarization in the Gaussian approximation [23] (it is also valid in the case of circular polarization as shown in the Appendix of Ref. [7]). From $I_F^{\mathrm{IPW}}=2\pi^2 cK\epsilon_\parallel/(L^2\epsilon_a\epsilon_\perp^{1/2})$ (W m^{-2}) we obtain

$$\xi(\delta)=\frac{\xi^{\mathrm{IPW}}}{1+\bar{\delta}/\delta}, \qquad (9)$$

where $\xi^{\mathrm{IPW}}=(\epsilon_\perp/\epsilon_\parallel)^{1/2}(L/\pi)$ is the coherence length in the IPW limit. This equation defines an intrinsic δ, $\bar{\delta}=2^{3/2}/\pi\simeq 0.90$. Since $\xi(\delta)$ is essentially the length over which the system averages the excitation, it should be compared with the characteristic length of the excitation—i.e., w_0. It follows from Eq. (9) that

$$\xi/w_0\sim 1/\delta \quad \text{if} \quad \delta\gg\bar{\delta}, \qquad (10)$$

$$\xi/w_0\sim 1 \quad \text{if} \quad \delta\ll\bar{\delta}. \qquad (11)$$

This ratio can be used to gauge the efficiency of the spatial averaging of the nonuniform excitation in the (x,y) plane.

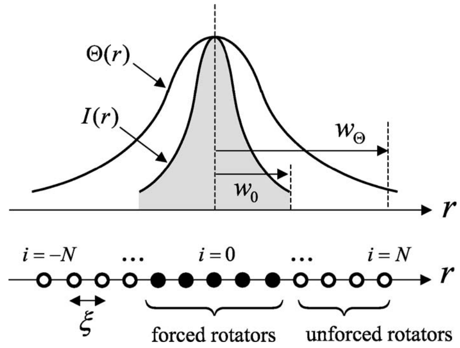

FIG. 12. Reduction of the initial problem, where the light intensity profile $I(r)$ and the reorientation profile $\Theta(r)$ have, respectively, a spatial extension w_0 and w_Θ, to a unidimensional finite set of rotators equally spaced by the distance ξ. Typically, the rotators located under the Gaussian light excitation ($r_i<w_0$) are forced (solid circles) by light angular momentum deposition to the medium while those located beyond w_0 are considered unforced (open circles).

The material response at a given position is expected to be local ($\xi/w_0\ll 1$) for large δ, whereas it depends on the state of the system in the surrounding region ($\xi/w_0\sim 1$) for small δ—i.e., a nonlocal behavior. Therefore $\bar{\delta}$ appears naturally as the parameter below which transverse nonlocal effects should be important and therefore identifies $\bar{\delta}$ as a relevant estimation of the critical value δ_c referred to previously.

The derivation of the exact system of equations governing the dynamics that accounts for a detailed description of the light-NLC system in the presence of the finite beam size effects is beyond the scope of this work. Our goal here is to extract the essential features of transverse nonlocal dynamical effects and to reduce the initial problem (a set of coupled partial differential equations involving all space coordinates and time) to a finite set of ordinary differential equations with respect to time. This can be achieved by the discretization procedure sketched in Fig. 12 where w_0 and w_Θ are the radii (at e^{-2}) of the light intensity and the reorientation profiles, respectively. The actual reorientation profile is not known and will not be calculated: it is assumed as a first guess to behave as $\Theta=\Theta_{\max}\exp(-2r^2/w_\Theta^2)\sin(\pi z/L)$ where $r^2=x^2+y^2$, $\Theta_{\max}$ is the amplitude of the lowest reorientation mode estimated at $r=0$, and the radius w_Θ is expressed as $w_\Theta=L(2^{1/2}\delta/\pi)^{1/2}$ as first derived in Ref. [23]. We then reduce the initial problem to a one-dimensional finite assembly of rotators at locations $r_i=i\xi$ where i is an integer running from $-N$ to N, with N defined as the integer part of the ratio w_Θ/ξ (Fig. 12). The reduced system consists of $2N+1$ coupled rotators represented by the pair of angles (Θ_i,Φ_i). Furthermore, recalling that since the details of the longitudinal (along the z axis) dynamics are presently of no concern, we restrict the dynamics of the rotators to their simplest form by imposing that the polar angles behave as

$$\Theta_i=\Theta_{\max}\exp(-2r_i^2/w_\Theta^2) \qquad (12)$$

and by ignoring any twisted modes of reorientation. We are therefore left with a system of coupled equations

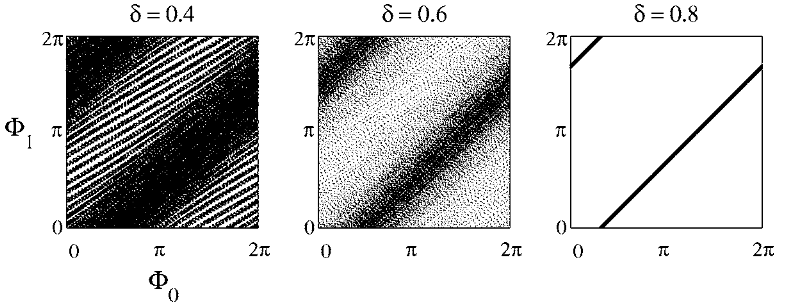

FIG. 13. Phase diagram Φ_1 as a function of Φ_0 for $\delta=0.4$, 0.6, and 0.8. Phase locking occurs at $\delta_c \simeq 0.70$. The normalized integration time is 500 times the period of the rotator located at $r=0$, the initial conditions are $\Phi_i=0$ for all i, and the transient has been removed. In each case, the total number of rotators is $2N+1=9$.

$$\frac{\partial \Phi_i}{\partial t} = \Omega_i + \sum_{\rm NN} f_{ij}(\delta), \tag{13}$$

where Ω_i is the forcing angular frequency of the precession of the ith rotator around the z axis imposed by the light angular momentum transfer to the NLC in the absence of an interaction with the other rotators. On the other hand, f_{ij} accounts for the coupling between the pair of nearest-neighbor (NN) rotators (i,j) (i.e., the elastic torque resulting from the local change of the director's orientation in the transverse direction) and will depend on the aspect ratio δ with the limiting behavior $f_{ij}(\delta \gg 1) \to 0$. These quantities are determined in what follows.

First, the forcing frequency Ω_i is expected to be proportional to the amount of angular momentum deposited by each photon, $(1-\cos\Delta_i)\hbar$, and to the photon flux, $I_i/(h\nu)$, at the location r_i. Δ_i is the phase shift experienced between the extraordinary and the ordinary waves after the light has passed through the sample at $r=r_i$, I_i is the light intensity at $r=r_i$, and ν is the light frequency. An expression for Ω_i can be inferred from knowledge of the IPW situation (at the OFT threshold) within the limit of small reorientation ($\Theta_{\rm max}^2 \ll 1$). In that case, $\Omega^{\rm IPW}=(1-\cos\Delta^{\rm IPW})/(\Delta^{\rm IPW}\tau_{\rm NLC})$ [24] with $\tau_{\rm NLC}=\gamma_1 L^2/(\pi^2 K)$ where γ_1 is the orientational viscosity. Moreover, $\Delta^{\rm IPW}=\tilde{L}\Theta_{\rm max}^{\rm IPW2}$, $\tilde{L}=L\pi\epsilon_a\epsilon_\perp/(2\epsilon_\parallel\lambda)$ being the normalized film thickness and typically $\Delta^{\rm IPW}\simeq\pi$ at the OFT threshold. Further extension of these results to the finite beam size case implies that one needs to take into account (i) the amplification factor for the OFT threshold intensity, $\rho_{\rm th}=[1+2^{3/2}/(\pi\delta)]^2$ [23], and (ii) the light intensity and reorientation profiles at $r=r_i$. Putting together gives the expression

$$\Omega_i = \frac{1-\cos\Delta_i}{\Delta_i \tau_{\rm NLC}}\rho_{\rm th}\exp(-2r_i^2/w_0^2), \tag{14}$$

where, from Eq. (12) and $\Delta_0=\pi$,

$$\Delta_i = \pi\exp(-4r_i^2/w_\Theta^2). \tag{15}$$

Second, since the intermolecular interactions in NLC are attractive, the molecules tend to align. In a simple scheme that preserves the symmetry $\boldsymbol{n}\to-\boldsymbol{n}$, we will thus consider that the jth rotator exerts on the ith a torque proportional to $(\boldsymbol{n}_i\cdot\boldsymbol{n}_j)(\boldsymbol{n}_i\times\boldsymbol{n}_j)$. In that case, the (azimuthal) coupling contribution to Eq. (13) reads

$$f_{ij} = g_{ij}(\boldsymbol{n}_i\cdot\boldsymbol{n}_j)(\boldsymbol{n}_i\times\boldsymbol{n}_j)_z,$$

where $g_{ij}>0$ (attraction). Dimensional arguments are useful for the determination of g_{ij}. It has the dimension of frequency and thus can be written as $g_{ij}=K/(\gamma_1\ell_{ij}^2)$ where ℓ_{ij} is a typical length associated with the pair (i,j), naturally taken as $\ell_{ij}=\xi$. Finally, using the normalized time $\tau=t/\tau_{\rm NLC}$, Eq. (13) becomes (in the limit $\Theta^2\ll 1$)

$$\frac{\partial\Phi_i}{\partial\tau} = \omega_i + \sum_{\rm NN}\Gamma_{ij}\sin(\Phi_j-\Phi_i), \tag{16}$$

where $\omega_i=\Omega_i\tau_{\rm NLC}$ are the normalized angular forcing frequencies and the coupling coefficients Γ_{ij} depend solely on δ following

$$\Gamma_{ij}(\delta) = \frac{\epsilon_\parallel}{\epsilon_\perp}\left[\frac{\xi^{\rm IPW}}{\xi(\delta)}\right]^2\Theta_i(\delta)\Theta_j(\delta), \tag{17}$$

where

$$\Theta_n(\delta) = (\pi/\tilde{L})^{1/2}\exp\left(-\frac{n^2\pi\sqrt{2}}{\delta}\frac{\xi^2}{L^2}\right). \tag{18}$$

The simulations have been done with the refractive indices $\epsilon_\parallel^{1/2}=1.75$ and $\epsilon_\perp^{1/2}=1.52$ corresponding to the NLC material E7 (from Merck datasheet) and taking for initial conditions $\Phi(\tau=0)=0$ for all i. For the purpose of demonstration, we focus our attention on the dynamics of the rotators located in the central part of the excitation beam—namely, $i=0$ and $i=\pm1$—by looking at the behavior of Φ_1 as a function of Φ_0 [note that the dynamics for $i=-1$ and $i=1$ are identical; see Eqs. (16)–(18)]. The results are shown in Fig. 13 where the phase diagrams have been plotted for $\delta=0.4$, 0.6, and 0.8. Above $\delta=0.8$ the situation is qualitatively unchanged with respect to the case $\delta=0.8$; i.e., a phase-locked regime is observed. Therefore Fig. 13 illustrates the existence of a critical value $\delta_c\simeq0.70$ that separates two distinct dynamics. For $\delta>\delta_c$ the central rotators are phase locked while for $\delta<\delta_c$ they are not. These results clearly indicate that a bifurcation has occurred at $\delta=\delta_c$, which is a generic behavior for coupled oscillators. Despite the fact that the proposed modelization has been based on physical grounds, it remains a toy model. Indeed, it consists of a collection of pure phase oscillators while the experiments correspond to both a phase (Φ) and amplitude (Θ) dynamics. Nevertheless, the fact that the critical value $\delta_c\simeq0.70$ corresponds approximately to the distinctive value $\bar{\delta}\simeq0.90$ that appears in the expression of the coherence length in Eq. (9)

invites us to connect the observation of new (with respect to the IPW limit) dynamical regimes when δ is sufficiently small (e.g., regimes R3 and R4) to transverse nonlocal manifestations.

IV. CONCLUSION

We have proposed an experimental method for the reconstruction of the director reorientation dynamics when a nematic liquid-crystal film is excited by light. We have demonstrated that a sequence of nonlinear rotations of the type "periodic → quasiperiodic → chaotic → quasiperiodic → periodic" takes place when the excitation beam is circularly polarized with a symmetric intensity profile. This bifurcation scenario is only observed when the beam diameter is sufficiently small compared to the cell thickness and is not predicted by available theoretical models.

It may be interesting to note that the system of equations (16) has the generic form of the well-known model of Kuramoto [25] (finite dimensional in our case), which was originally introduced to describe oscillatory chemical reactions. A recent review dedicated to the analysis of synchronization phenomena on the basis of the Kuramoto model can be found in [26]. Although the present model can claim only to give a first simple (pure phase oscillators) picture of dynamical transverse nonlocal effects in optically excited NLC films, some results on the collective behavior of limit-cycle oscillators encourage us to include amplitude dynamics in our approach. For instance, Matthews and Strogatz [27] have shown that linearly coupled oscillators with amplitude and phase degrees of freedom near a Hopf bifurcation exhibit unsteady dynamics (i.e., large-amplitude oscillations, quasiperiodicity, chaos) in well-defined regions of the coupling strength and a spread of the natural frequencies. In our context, this should be associated with the observation of the chaotic regime, R3, and the quasiperiodic regime with large-amplitude oscillations, R4. A more recent example concerns the observation of a high-dimensional chaotic behavior, called phase chaos, in the finite-dimensional Kuramoto model of coupled limit-cycle, or chaotic, oscillators [28].

ACKNOWLEDGMENTS

We would like to thank T. V. Galstian for access to his experimental facilities at the Center for Optics and Laser, Laval University, Québec, Canada. E.B. is grateful to A. Vella for useful clarifications of her work.

---

[1] D. O. Krimer, L. Kramer, E. Brasselet, T. V. Galstian, and L. J. Dubé, J. Opt. Soc. Am. B **22**, 1681 (2005).
[2] A. Vella, A. Setaro, B. Piccirillo, and E. Santamato, Phys. Rev. E **67**, 051704 (2003).
[3] G. Demeter, D. O. Krimer, and L. Kramer, Phys. Rev. E **72**, 051712 (2005).
[4] M. G. Rosenblum, A. S. Pikovsky, and J. Kurths, Phys. Rev. Lett. **76**, 1804 (1996).
[5] A. Pikovsky, M. Rosenblum, and J. Kurths, *Synchronization: A Universal Concept in Nonlinear Sciences* (Cambridge University Press, Cambridge, England, 2003).
[6] Y.-C. Lai, D. Armbruster, and E. J. Kostelich, Phys. Rev. E **62**, R29 (2000); A. Pikovsky and M. Rosenblum, *ibid.* **64**, 058203 (2001); Y.-C. Lai, D. Armbruster, and E. J. Kostelich, *ibid.* **64**, 058204 (2001).
[7] E. Brasselet, B. Doyon, T. V. Galstian, and L. J. Dubé, Phys. Rev. E **69**, 021701 (2004).
[8] S. D. Durbin, S. M. Arakelian, and Y. R. Shen, Opt. Lett. **6**, 411 (1981).
[9] E. Brasselet, T. V. Galstian, L. J. Dubé, D. O. Krimer, and L. Kramer, J. Opt. Soc. Am. B **22**, 1671 (2005).
[10] G. Russo, V. Carbone, and G. Cipparrone, Phys. Rev. E **62**, 5036 (2000).
[11] H. Kantz and T. Schreiber, *Nonlinear Time Series Analysis*, 2nd ed. (Cambridge University Press, Cambridge, England, 2004).
[12] F. Takens, Lect. Notes Math. **898**, 366 (1981).
[13] T. Sauer, J. A. Yorke, and M. Casdagli, J. Stat. Phys. **65**, 579 (1991).
[14] T. Schreiber, Phys. Rev. E **47**, 2401 (1993).
[15] M. T. Rosenstein, J. Collins, and C. D. Luca, Physica D **65**, 117 (1993).
[16] H. Kantz, Phys. Lett. A **185**, 77 (1994).
[17] G. Cipparrone, V. Carbone, C. Versace, C. Umeton, R. Bartolino, and F. Simoni, Phys. Rev. E **47**, 3741 (1993).
[18] A. S. Zolot'ko, V. F. Kitaeva, N. N. Sobolev, V. Y. Fedorovich, A. P. Sukhorukov, N. Kroo, and L. Csillag, Liq. Cryst. **15**, 787 (1993).
[19] E. Santamato, P. Maddalena, L. Marrucci, and B. Piccirillo, Liq. Cryst. **25**, 357 (1998).
[20] B. Piccirillo, C. Toscano, F. Vetrano, and E. Santamato, Phys. Rev. Lett. **86**, 2285 (2001).
[21] E. Brasselet, A. Lherbier, and L. Dubé, J. Opt. Soc. Am. B **23**, 36 (2006).
[22] In this expression the factor of 2 accounts for an effective intensity acting on the NLC at the OFT threshold in the circular polarization case that corresponds to the extraordinary part only, which is half the total intensity.
[23] A. S. Zolot'ko, V. F. Kitaeva, V. Kuyumchyan, N. Sobolev, A. Sukhorukov, and L. Csillag, Pis'ma Zh. Eksp. Teor. Fiz. **36**, 66 (1982) [JETP Lett. **36**, 80 (1982)].
[24] L. Marrucci, G. Abbate, S. Ferraiuolo, P. Maddalena, and E. Santamato, Phys. Rev. A **46**, 4859 (1992).
[25] Y. Kuramoto, in *International Symposium on Mathematical Problems in Theoretical Physics*, edited by H. Araki, Lecture Notes in Physics, Vol. 30 (Springer, New York, 1975), p. 420.
[26] J. Acebrón, L. Bonilla, C. P. Vicente, F. Ritort, and R. Spigler, Rev. Mod. Phys. **77**, 137 (2005).
[27] P. C. Matthews and S. H. Strogatz, Phys. Rev. Lett. **65**, 1701 (1990).
[28] O. V. Popovych, Y. L. Maistrenko, and P. A. Tass, Phys. Rev. E **71**, 065201(R) (2005).